Vortex Dynamics and Fractal Structures in Reactive Richtmyer-Meshkov Instability

M. Bambauer[a], J. Hasslberger[a], N. Chakraborty[b] & M. Klein[a]

[a] Bundeswehr University Munich, Department of Aerospace Engineering, Germany
[b] Newcastle University, School of Engineering, United Kingdom

E-mail: *maximilian.bambauer@unibw.de*

Abstract

In nuclear and process plant safety, the accurate prediction of explosion loads requires understanding of various mechanisms responsible for flame acceleration (FA) and deflagration-to-detonation transition (DDT). In confined geometries, shock-flame interactions due to shock reflections at obstacles and walls are a key contributing factor to FA and DDT. In this context, the wrinkling of the flame surface due to the production of baroclinic torque and in consequence the increase of the integral reaction rate is referred to as the reactive Richtmyer-Meshkov Instability (RMI).

With the goal of developing a RMI sub-grid model, compressible 3D-DNS of a shock-flame interaction in a lean and a stoichiometric homogeneous H2/Air mixture have been performed. The chemistry is modeled using a modified one-step Arrhenius approach, since the problem is dominated by fluid dynamic phenomena rather than complex chemical kinetics. Temporal and spatial discretization are achieved using a 3rd order Runge-Kutta method and a high-order WENO scheme respectively. The set-up consists of a planar shock propagating towards a perturbed but statistically planar flame. After interacting with the flame, the shock is reflected at the back-end of the domain, causing a second shock-flame interaction (re-shock).

The development of the RMI, measured by the evolution of the flame surface area and turbulent mixing width, is influenced by key physical parameters. One important parameter is the equivalence ratio, as it affects the Lewis number and laminar flame speed. Using the DNS database, sub-grid modeling approaches for closure of the averaged/filtered reaction rate can be quantified. For this purpose individual terms of the enstrophy transport equation are analyzed, identifying dominant mechanisms during the development of the instability. Furthermore, the fractal behavior of the RMI is analyzed in an approach of power-law based modeling of the flame wrinkling factor.

For the investigated cases it is found that the baroclinic torque is the most dominant enstrophy transport term, showing high peaks after every shock-flame interaction. The baroclinic torque is heavily dependent on the flame thickness, which varies with the chosen equivalence ratio and in time, as the flame thickness is reduced by about 50% after interacting with the shock and re-shock. Each shock interaction also causes a strong increase of the flame surface area and turbulent mixing width, with an maximum increase in area of about 400%. The final area increase of the stoichiometric case is about 30% lower than the lean case due to funnel-closure and smoothing effects, caused by the increased reaction rate. The fractal dimension D_f, as found in power law based modeling, is investigated using explicit filtering of the present DNS data. There a maximum fractal dimension of 2.92 to 2.96 is determined for both cases, before the stoichiometric and lean cases settle at a value of 2.38 and 2.67 respectively. Since the maximum fractal dimension of the flame surface is expected to be $8/3$ for a premixed flame, values of $D_\mathrm{f} > 8/3$ are a strong indicator for additional wrinkling caused by the RMI. For the lean case with an effective Lewis number $\mathrm{Le}_\mathrm{eff} < 1$, thermo-diffusive instabilities can provide an additional contribution towards flame wrinkling.

Keywords: *RMI, DNS, shock, vorticity, fractal, sub-grid model*

1 Introduction

The Richtmyer-Meshkov instability (RMI) (Richtmyer, 1960, Meshkov, 1972), like the Rayleigh-Taylor instability (RTI) (Rayleigh, 1882, Taylor, 1950), describes a form of hydrodynamic instability, that can occur at the interface between a light and heavy fluid upon interaction with a pressure gradient ∇p. In the RMI, the pressure gradient is caused by a shock wave, while in the case of RTI it is caused by constant acceleration $\mathbf{g}$ (e.g. gravity). The mechanism causing this type of instability is the production of vorticity, due to the misalignment of ∇p and the density gradient $\nabla \rho$ across the interface. Small disturbances at the fluid interface are increasingly amplified, leading to wrinkling and increased mixing of heavy and light fluid.

Two prominent occurrences for RMI and RTI in nature and technology are supernovae (Remington et al., 2000) and inertial confinement fusion (Lindl, 1995). The focus of this work lies on the RMI in the context of combustion, where it plays an important role as a mechanism for the deflagration-to-detonation transition (DDT) in geometrically confined explosions. In that context, the RMI is caused by a shock wave interacting with a flame (density gradient), after being reflected from an obstacle or wall (Ciccarelli et al., 2010). The RMI causes a heavily wrinkled flame brush region and subsequently a strong increase in the integral reaction rate, which can be a decisive factor for DDT (Dorofeev, 2011). Understanding and accurate prediction of the DDT and explosion loads is a key element in nuclear and chemical safety research (Breitung et al., 2000). Commercial applications can only provide qualitative predictions of explosion loads in large scale geometries due to the heavy computational demands posed by the wide time- and length-scale spectrum, associated with the simulation of the chemistry and turbulent flow in such cases (Ciccarelli and Dorofeev, 2008). The accuracy of large eddy simulation (LES) or unsteady Reynolds-averaged Navier-Stokes simulation (URANS) could be improved by including small-scale RMI effects via a sub-grid model (Hasslberger, 2017).

In this work direct numerical simulations (DNS) of shock-flame interactions for a lean and stoichiometric H2/Air gas mixture are presented and analyzed in regards of $A_\mathrm{f}(t)$, $\delta_\mathrm{w}(t)$, the enstrophy transport equation and fractal behavior for power law based modeling of the flame wrinkling. Sec. 2 will give an overview on the numerical methods used for the DNS simulations, which is followed by an explanation of the case set-up in sec. 3. The simulation results are presented in sec. 4 with an analysis of the enstrophy transport equation in sec. 4.1 and of the fractal flame wrinkling in sec. 4.2.

2 Numerical Methods

The SENGA solver (Jenkins and Cant, 1999) is used to carry out 3D combustion DNS of the shock-flame interactions. It solves a dimensionless form of the Navier-Stokes (NS) equations, including the total energy e_t and reaction progress variable c, given by Eqs. (1) to (4) and using the dimensionless variables defined in table 1.

$$\frac{\partial \rho}{\partial t} + \frac{\partial (\rho u_k)}{\partial x_k} = 0 \tag{1}$$

$$\frac{\partial (\rho u_i)}{\partial t} + \frac{\partial (\rho u_k u_i)}{\partial x_k} = -\frac{\partial p}{\partial x_i} + \frac{1}{\mathrm{Re}_0}\frac{\partial \tau_{ki}}{\partial x_k} \tag{2}$$

$$\begin{aligned}\frac{\partial (\rho e_t)}{\partial t} + \frac{\partial (\rho u_k e_t)}{\partial x_k} = &-(\gamma-1)\mathrm{M}_0^2\frac{\partial (p u_k)}{\partial x_k} + \frac{1}{\mathrm{Re}_0}(\gamma-1)\mathrm{M}_0^2\frac{\partial (\tau_{ki}u_i)}{\partial x_k} \\ &+ \frac{\tau_\mathrm{h}}{\mathrm{Re}_0\mathrm{Pr}}\frac{\partial}{\partial x_k}\left[\lambda\frac{\partial T}{\partial x_k}\right] - \frac{\tau_\mathrm{h}}{\mathrm{Re}_0\mathrm{LePr}}\frac{\partial}{\partial x_k}\left[\rho D\frac{\partial c}{\partial x_k}\right]\end{aligned} \tag{3}$$

$$\frac{\partial (\rho c)}{\partial t} + \frac{\partial (\rho u_k c)}{\partial x_k} = \dot{\omega} + \frac{1}{\mathrm{Re}_0\mathrm{LePr}}\frac{\partial}{\partial x_k}\left[\rho D\frac{\partial c}{\partial x_k}\right] \tag{4}$$

The dimensioned (superscript '*') reference (subscript '0') values for density ρ_0^*, temperature T_0^*, thermal conductivity λ_0^*, mass diffusivity D_0^*, specific heat capacities $c_{\mathrm{p},0}^*$ and $c_{\mathrm{v},0}^*$, dynamic viscosity μ_0^* and the adiabatic flame temperature T_ad^* are taken from the initial state (unburned H2/Air gas-

***Table 1**: Definition of the dimensionless variables.*

variable	**definition**
density	$\rho = \rho^* / \rho_0^*$
pressure	$p = p^* / (\rho_0^* u_0^{*2})$
temperature	$T = (T^* - T_0^*) / (T_{\mathrm{ad}}^* - T_0^*)$
velocity	$u_i = u_i^* / u_0^*$
thermal conductivity	$\lambda = \lambda^* / \lambda_0^*$
mass diffusivity	$D = D^* / D_0^*$
total chemical energy	$e_{\mathrm{t}} = e_{\mathrm{t}}^* / (c_{\mathrm{p},0}^* T_0^*)$
viscous stress	$\tau = (\tau^* l_0^*) / (\mu_0^* u_0^*)$
length	$x_i = x_i^* / l_0^*$
time	$t = t^* u_0^* / l_0^*$

mixture) at $t^* = 0$. The reference velocity u_0^* and reference length l_0^* are set to the laminar burning velocity S_{L} and to $\approx 250\delta_{\mathrm{th,st}}^*$ (thermal laminar flame thickness for stoichiometric mixture at $t^* = 0$) respectively.

Using the heat capacity ratio $\gamma = c_{\mathrm{p},0}^* / c_{\mathrm{v},0}^*$ and the specific gas constant R_{s}^*, the reference speed of sound can be defined as $a_0^* = \sqrt{\gamma R_s^* T_0^*}$. This gives a reference Mach number of $M_0 = u_0^* / a_0^*$. Other dimensionless parameters such as the reference Reynolds number Re_0, Prandtl number Pr, Schmidt number Sc, Lewis number Le and heat release parameter τ_{h} are defined as:

$$\mathrm{Re}_0 = \frac{\rho_0^* u_0^* l_0^*}{\mu_0^*} \quad \mathrm{Pr} = \frac{\mu_0^* c_{\mathrm{p},0}^*}{\lambda_0^*} \quad \mathrm{Sc} = \frac{\mu_0^*}{\rho_0^* D_0^*} \quad \mathrm{Le} = \frac{\lambda_0^*}{\rho_0^* D_0^* c_{\mathrm{p},0}^*} \quad \tau_{\mathrm{h}} = \frac{T_{\mathrm{ad}}^* - T_0^*}{T_0^*} \tag{5}$$

The parameters Re_0 and M_0 are calculated using $u_0^* = S_{\mathrm{L}}$ as per definition of the reference parameter u_0^*. Since the RMI is mainly dominated by the dynamics of the shock-flame interaction and a detailed chemistry model would entail large computational costs, the chemistry (see $\dot{\omega}$ in Eq. (4)) is modeled using the following one step Arrhenius approach.

$$\dot{\omega} = B_{\mathrm{A}} \rho (1 - c) \exp\left[- \frac{\beta_{\mathrm{z}} (1 - T)}{1 - \alpha_{\mathrm{h}} (1 - T)} \right] \tag{6}$$

The Zeldovich number β_{z} and parameter α_{h} are defined as $\beta_{\mathrm{z}} = T_{\mathrm{ac}}^* (T_{\mathrm{ad}}^* - T_0^*) / T_{\mathrm{ad}}^{*2}$ and $\alpha_{\mathrm{h}} = \tau_{\mathrm{h}} / (1 + \tau_{\mathrm{h}})$, where T_{ac}^* is the activation temperature. The values used in the present cases for β_{z} and the pre exponential factor B_{A} can be found in table 2. The viscous stress tensor τ_{ki} is defined as:

$$\tau_{ki} = \mu \left[\frac{\partial u_i}{\partial x_j} + \frac{\partial u_j}{\partial x_i} \right] - \frac{2}{3} \delta_{ij} \left[\frac{\partial u_k}{\partial x_k} \right] \tag{7}$$

For time discretization a low-storage third-order explicit Runge-Kutta scheme (Wray, 1990) is utilized. The spatial derivatives of all convective terms are calculated with the fifth order WENO-5 method by Jiang and Shu (1996), using the scalar Lax-Friedrichs flux splitting procedure described by Shu (1998). At the non-periodic boundaries, the scheme is gradually reduced to a one-sided 2nd order scheme. The scheme provides sharp shock capturing capabilities without numerical oscillations for the investigated cases. Figure 1 shows a comparison of the WENO-5 scheme with an analytical 1D solution of a shock at a shock Mach number of $M_{\mathrm{s}} = 1.5$, where the shock is resolved by about 2-3 nodes. All simulations presented in this work are initialized with a $M_{\mathrm{s}} = 1.5$ shock, without expansion fan and contact discontinuity.

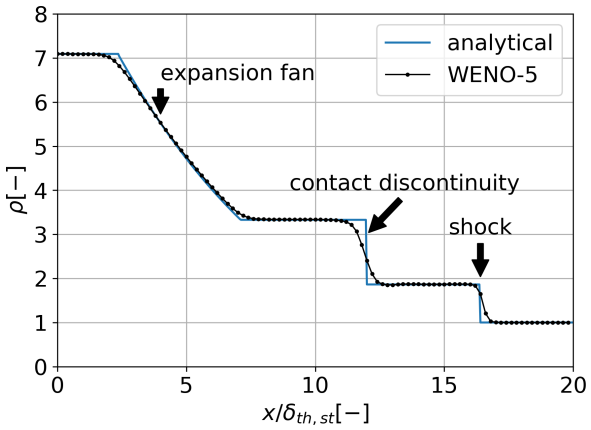

***Fig. 1**: Comparison of the numerical and analytical shock-tube solution for $M_s = 1.5$.*

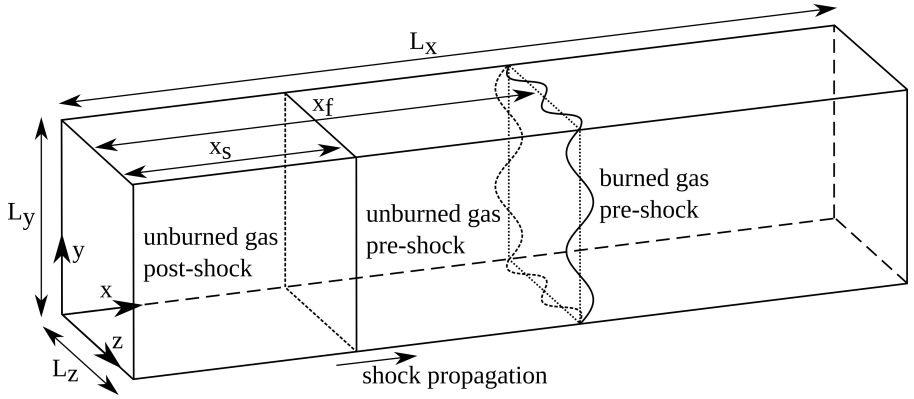

***Fig. 2**: Set-up schematic with position of shock and statistically planar flame.*

3 Simulation Set-Up

The simulation domain, consisting of a rectangular channel divided into areas of unburned and burned gas by a statistically planar flame, is schematically shown in Fig. 2. Figure 3 depicts the boundary conditions used in the set-up. A modified Navier-Stokes characteristic boundary condition (NSCBC) is implemented at $x = 0$ to allow for both outflow and inflow of fluid (Poinsot and Veynante, 2005). To enable the reflection of incoming shock waves, an adiabatic free-slip boundary is applied at $x = L_x$. The remaining boundaries in y and z-direction are periodic. The RMI can only occur if an initial disturbance is present in the flame surface. A flame disturbance method by Tritschler et al. (2013) is used for this purpose. It enables a quasi-stochastic disturbance of the flame front while still remaining reproducible on different systems, i.e. it is not based on random numbers. Across all cases in this work the initial flame disturbance was kept constant. The disturbance field, is shown in Fig. 4, with the initial displacement in x-direction for each point of the statistically planar flame surface.

For the present work, two cases of a H2/Air gas mixture at different equivalence ratios ϕ are inves-

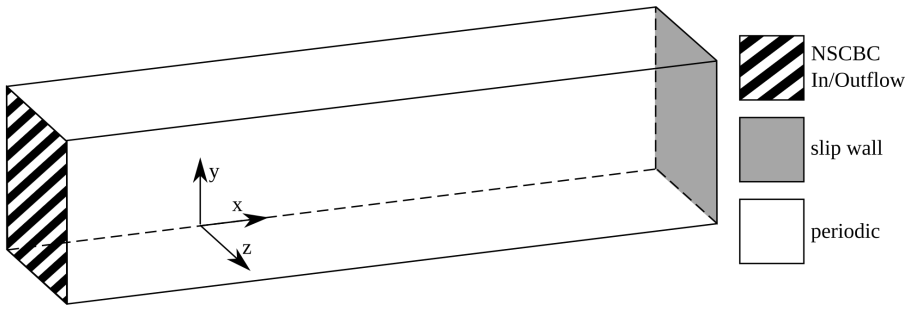

***Fig. 3**: Set-up schematic showing the boundary conditions.*

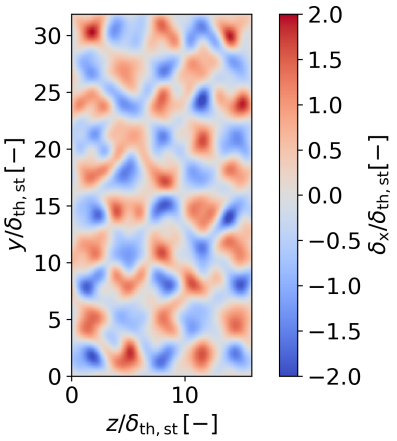

***Fig. 4**: Distortion δ_{x} of the statistically planar flame front.*

***Table 2**: Input parameters for simulation cases.*

	stoichiometric	**lean**
ϕ	1.0	0.5
Le	1.1	0.5
Re_0	1093	213
Pr	0.47	0.52
Sc	0.52	0.26
τ_{h}	7.1	4.5
β_{z}	5.0	5.0
M_0	0.005609	0.001025
M_{s}	1.5	1.5
B_{A}	50000	13000

tigated. The set-up parameters listed in Tab. 2 for the stoichiometric case ($\phi = 1$) and the lean case ($\phi = 0.5$) were calculated using the Cantera software (Goodwin et al., 2018) and the GRI-MECH 3.0 model at $T_0^* = 298.15\,\mathrm{K}$ and $p_0^* = 1\,\mathrm{bar}$. Changing ϕ has an effect on several important parameters, such as the laminar flame speed S_{L}, the heat release parameter τ_{h}, the density gradient of the flame $\nabla\rho$ and the Lewis number. Generally, the Lewis number (see Eq. (5)) is calculated using the mass diffusion coefficient of the deficient reactant. For a very lean mixture ($\phi \ll 1$) the Hydrogen-Lewis number is $\mathrm{Le}_{\mathrm{H2}} \approx 0.3$ and for a very fuel-rich mixture ($\phi \gg 1$) the Oxygen-Lewis number is $\mathrm{Le}_{\mathrm{O2}} \approx 2.1$. To avoid a jump of the Lewis number at $\phi = 1$, an effective (also known as reduced) Lewis number $\mathrm{Le}_{\mathrm{eff}}$ is defined, that provides a smooth transition between $\mathrm{Le}_{\mathrm{H2}}$ and $\mathrm{Le}_{\mathrm{O2}}$ in the whole ϕ range. The definition of the effective Lewis number used in this work can be found in Bechtold and Matalon (2001) and is calculated from the Cantera results with

$$\mathrm{Le}_{\mathrm{eff}} = 1 + \frac{(\mathrm{Le}_{\mathrm{H2}} - 1) + (\mathrm{Le}_{\mathrm{O2}} - 1)A_{\mathrm{Le}}}{1 + A_{\mathrm{Le}}}, \tag{8}$$

where $A_{\mathrm{Le}} = 1 + \beta_{\mathrm{z}}(\Phi - 1)$ and $\Phi = \phi$ for fuel-rich mixtures and $\Phi = 1/\phi$ for lean-mixtures. For the sake of simplicity the following text will refer to the effective Lewis number only as "Lewis number" or Le.

The normalized flame area $A_{\mathrm{f}}/A_{\mathrm{f,n}}$ and the normalized turbulent mixing width $\delta_{\mathrm{m}}/\delta_{\mathrm{m,n}}$, obtained from the DNS, can be related to the wrinkling factor and turbulent diffusion, which is required for LES or URANS sub-grid modeling. There they can provide insights in modeling approaches for closure of the reaction rate term, or the non-linear convective term. For A_{f}(Klein et al., 2020) and δ_{m} (Tritschler et al., 2014) the following definitions are used.

$$A_\mathrm{f} = \iiint_V |\nabla c| dV \tag{9}$$

$$\delta_\mathrm{m} = \int_0^{L_\mathrm{x}} 4\langle c\rangle(1-\langle c\rangle)dx \tag{10}$$

$$\langle c\rangle = \frac{1}{L_\mathrm{y}L_\mathrm{z}} \iint c\, dydz \tag{11}$$

With $\delta_{\mathrm{th,st}}$ as the thermal laminar flame thickness of the stoichiometric case, the dimensions of the domain are $L_\mathrm{x} \times L_\mathrm{y} \times L_\mathrm{z} = 128\delta_{\mathrm{th,st}} \times 32\delta_{\mathrm{th,st}} \times 16\delta_{\mathrm{th,st}}$ uniformly discretized by $1024 \times 256 \times 128$ grid points. The shock and flame are initialized at $x_\mathrm{s} = 3.125\delta_{\mathrm{th,st}}$ and $x_\mathrm{f} = 12.5\delta_{\mathrm{th,st}}$ respectively. The initial thermal laminar flame thickness of the lean case is $\delta_{\mathrm{th,le}} \approx 8\delta_{\mathrm{th,st}}$.

4 Results

Figure 5 shows density slices in the xy-plane at successive timesteps for the stoichiometric and lean case. The subfigures Fig. 5a to Fig. 5d show the formation of fresh gas funnels reaching into the burned side of the gas, after the first shock-flame interaction at $t \times S_{\mathrm{L,st}}/\delta_{\mathrm{th,st}} = 0.2$. Then at $t \times S_{\mathrm{L,st}}/\delta_{\mathrm{th,st}} = 0.4$, a second shock-flame interaction ('re-shock') occurs, after the shock has been reflected from the back wall of the domain. Next at $t \times S_{\mathrm{L,st}}/\delta_{\mathrm{th,st}} = 0.6$, another shock flame interaction occurs (termed 'reflection'), caused by partial transmissions and reflections of the shock between the flame surface and the back wall after re-shock. Finally another interaction with a partially reflected shock occurs at $t \times S_{\mathrm{L,st}}/\delta_{\mathrm{th,st}} = 0.8$. As time progresses differences between both cases in the development of the fresh gas funnels and later the overall structure of the flame surface become apparent. The laminar flame speed for $\phi = 1$ is about five times higher than for $\phi = 0.5$. This leads to an increased reduction in size of the fresh gas funnels for the stoichiometric case, as the funnels and other developing turbulent structures are continuously being enclosed by reacting gas. The effects of this on later development of the flame surface structure, can be seen in Fig. 5d. In the lean case the flame surface shows a variety of small scale wrinkled structures, which are not present in the stoichiometric case.

Another contributing factor to the differences in the development of the flame brush for both cases are the differences in Lewis number. In the lean case the formation of thermo-diffusive instabilities are promoted by the low Lewis number which contributes to the flame wrinkling in addition to the RMI. The shock-position offset is caused by differences in the speed of sound, due to an increased adiabatic flame temperature in the stoichiometric case and differences in the turbulent mixing width.

Figure 6 shows the temporal development of the normalized flame surface area A_f and normalized turbulent mixing width δ_m for the stoichiometric ($\phi = 1$) and lean ($\phi = 0.5$) case. The flame area is normalized with the area of the shock tube cross-section $A_{\mathrm{f,n}}$. For $\delta_{\mathrm{m,n}}$ the initial mixing width of the $\phi = 1$ case at $t \times S_{\mathrm{L,st}}/\delta_{\mathrm{th,st}} = 0$ is taken. After each shock interaction, an area increase is observed for both cases. The stoichiometric case shows a steep linear increase at the beginning of the first shock interaction, growing faster than the lean case. Since the initial flame perturbation is the same for both cases, this is caused by the increased initial density gradient across the flame due to the lower flame thickness (see Fig. 8) and the increased heat release parameter τ_h for $\phi = 1$. As is shown in sec. 4.1, this leads to a higher production of baroclinic torque and increased wrinkling. The flame surface area then reaches a maximum increase of about 300%, before decreasing slightly again until the interaction with the re-shock. The area decrease is caused by the closure of the fresh gas funnels by the burning gas and further smoothing of emerging turbulent structures. The funnel-closure and smoothing effects are far less pronounced for the lean case, therefore it surpasses the stoichiometric case in area after the re-shock. The final surface area values reached at $t \times S_{\mathrm{L,st}}/\delta_{\mathrm{th,st}} = 1$ differ by about 30% between both cases. Another effect, which is visible for both A_f and δ_m, is a short initial decline when an interaction with a shock wave occurs. This is not connected with the RMI itself, but caused by the shock interacting with the leading flame structures first, before interacting with the rest

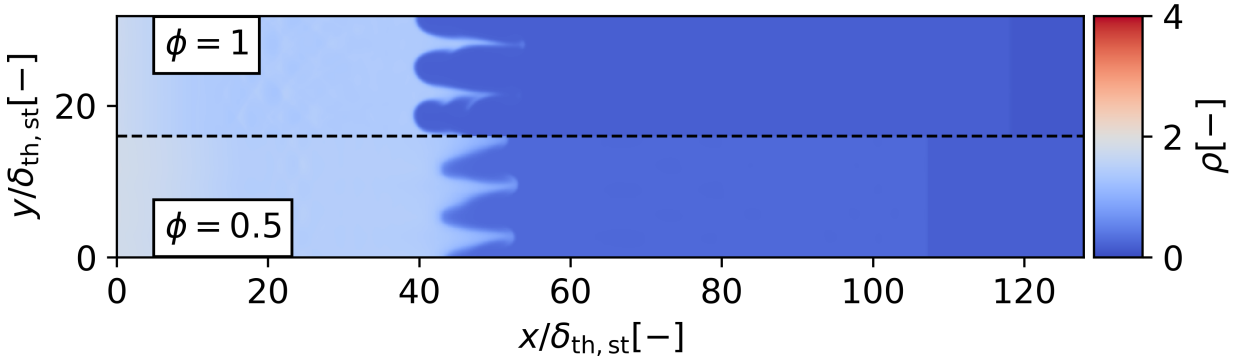

(a) Density slice at $t \times S_{\mathrm{L,st}}/\delta_{\mathrm{th,st}} = 0.2$; formation of fresh gas funnels after first shock-flame interaction.

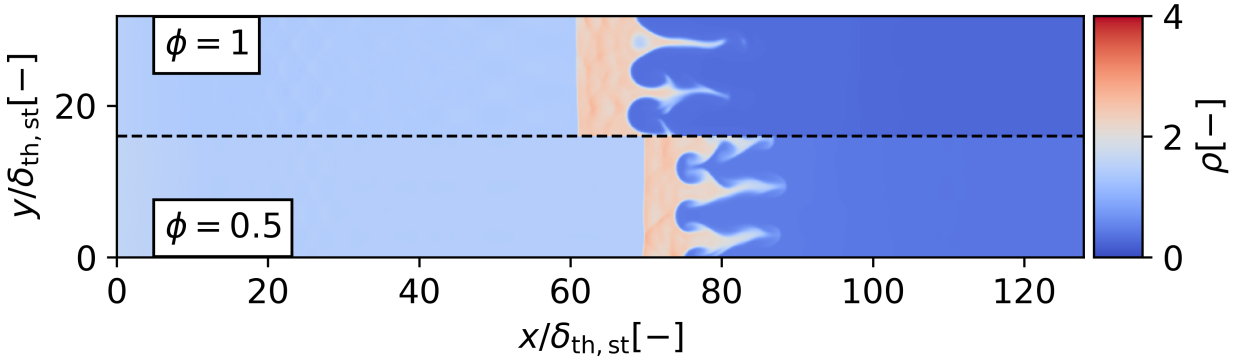

(b) Density slice at $t \times S_{\mathrm{L,st}}/\delta_{\mathrm{th,st}} = 0.4$; second shock-flame interaction (re-shock).

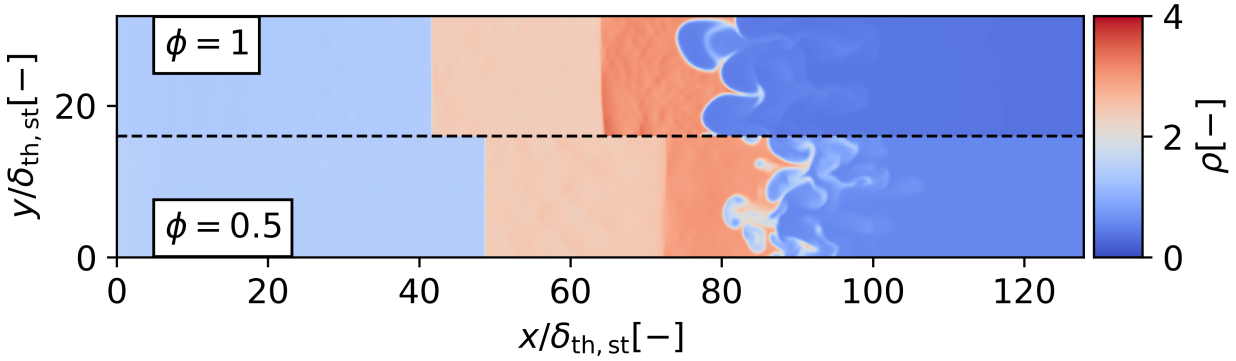

(c) Density slice at $t \times S_{\mathrm{L,st}}/\delta_{\mathrm{th,st}} = 0.6$; third shock-flame interaction (1st reflection).

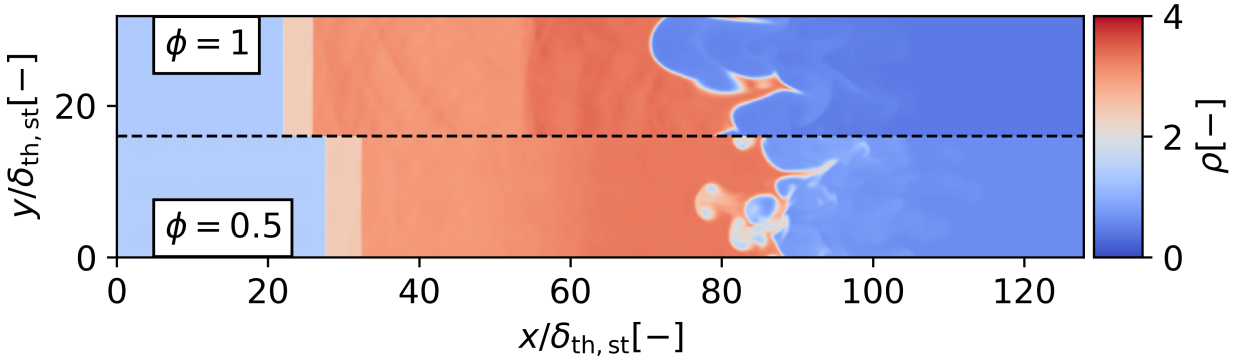

(d) Density slice at $t \times S_{\mathrm{L,st}}/\delta_{\mathrm{th,st}} = 0.8$; fourth shock-flame interaction (2nd reflection).

***Fig. 5**: Density slice of the shock tube at $z = L_z/2$ for successive timesteps. Comparison of equivalence ratio for stoichiometric ($\phi = 1$) and lean ($\phi = 0.5$) H2/Air gas mixture.*

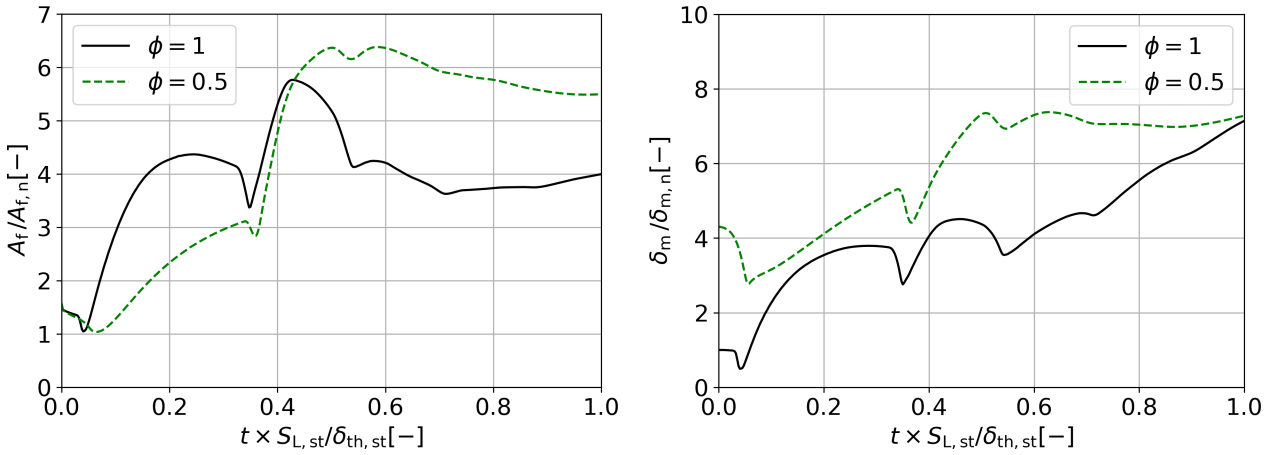

(a) Normalized flame surface area. *(b) Normalized mixing width.*

***Fig. 6**: Normalized flame surface area and normalized turbulent mixing width over time for lean and stoichiometric gas mixture.*

of the flame (and RMI sets on). Those structures are then flattened or pushed back, initially reducing A_f and δ_m.

Proceeding with the turbulent mixing width shown in Fig. 6b, it becomes apparent that the initial δ_m differs between both cases due to differences in flame thickness δ_f. The flame thickness δ_f is defined by $\delta_\mathrm{f} = V_\mathrm{f}/A_\mathrm{f}$, where the flame volume V_f is calculated by summation of all grid points with $0.01 \leq c \leq 0.99$. The normalization parameter $\delta_{\mathrm{f,n}}$ is taken for $\phi = 1$ and $t \times S_{\mathrm{L,st}}/\delta_{\mathrm{th,st}} = 0$ and $\delta_{\mathrm{f,n}} \approx 1.76\delta_{\mathrm{th,st}}$. Initially the flame thickness of the lean case is about eight times higher than for the stoichiometric case, resulting in an increased δ_m at the start of the simulation (see Fig. 8). In both cases the turbulent mixing width in Fig. 6b initially grows linearly after each shock flame interaction. While the lean case continues to grow in a linear fashion until the next shock interaction, the stoichiometric case reaches a maximum before it plateaus or even begins to decline (similar to Fig. 6a). Towards the end of the simulation the turbulent mixing width of the stoichiometric case keeps increasing steadily while δ_m starts to settle for the lean case. The continued growth could be explained by the increased reaction rate at $\phi = 1$, that causes large areas of burned gas to expand into the unburned gas as visible in Fig. 5d.

4.1 Enstrophy Analysis

The generation of vorticity due to baroclinic torque at the flame surface, is the main mechanism responsible for the RMI. The enstrophy $\Omega = \omega_i^2/2$ can be interpreted as a scalar energy equivalent of the vorticity $\omega_i = \varepsilon_{ijk}\partial u_k/\partial x_j$ and its transport equation is given as:

$$\frac{\partial \Omega}{\partial t} + u_k\frac{\partial \Omega}{\partial x_k} = \underbrace{\omega_i\omega_k\frac{\partial u_i}{\partial x_k}}_{\mathrm{T_I}} \underbrace{-\varepsilon_{ijk}\omega_i\frac{1}{\rho^2}\frac{\partial \rho}{\partial x_j}\frac{\partial \tau_{kl}}{\partial x_l}}_{\mathrm{T_{II}}} + \underbrace{\frac{\varepsilon_{ijk}\omega_i}{\rho}\frac{\partial^2 \tau_{kl}}{\partial x_j \partial x_l}}_{\mathrm{T_{III}}} \underbrace{-2\frac{\partial u_k}{\partial x_k}\Omega}_{\mathrm{T_{IV}}} + \underbrace{\varepsilon_{ijk}\frac{\omega_i}{\rho^2}\frac{\partial \rho}{\partial x_j}\frac{\partial p}{\partial x_k}}_{\mathrm{T_V}} \tag{12}$$

The terms on the right hand side represent the changes in enstrophy due to vortex stretching (I), viscous torque (II), diffusion (III), dilatation (IV) and baroclinic torque (V). The normalized volume integrals of the terms I to V are shown in Fig. 7 for the lean and stoichiometric case. Generally peaks in the enstrophy terms can be observed after each shock interaction. Term V (baroclinic torque) is dominating most of the time for both cases, although the peak heights differ in comparison. Term I (vortex stretching), term III (diffusion) and term IV (dilatation) show small peaks on each shock-flame interaction. Comparing the behavior of term I and term III in figs. 7a and 7b, a noticeable difference between the cases becomes apparent. After each shock interaction the terms decline again,

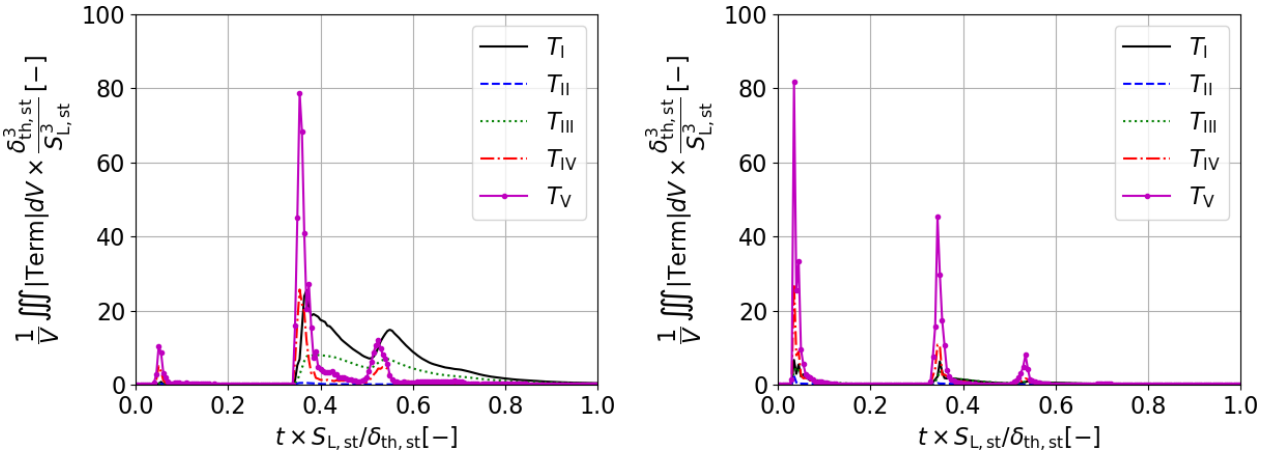

(a) $\phi = 0.5$ *(b)* $\phi = 1$

Fig. 7*: Normalized volume integral (with* $V = \mathrm{L_x L_y L_z}$*) of the enstrophy transport terms for lean and stoichiometric gas mixture.*

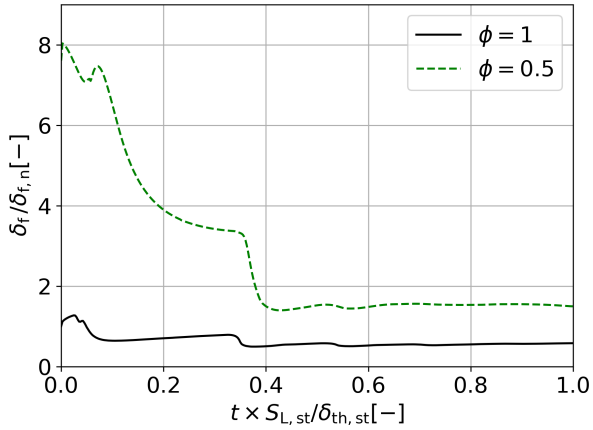

Fig. 8*: Normalized flame thickness over time for lean and stoichiometric gas mixture.*

but at a much slower rate than the baroclinic torque (term V), which causes terms I and III to become the dominant terms after the re-shock and the reflection. This can be seen for $\phi = 0.5$ and to a lesser extent for $\phi = 1$ as the values reached for term I and III are generally much smaller in this case. The influence of Term II (viscous torque) on the enstrophy production can be neglected for the investigated cases.

Focusing on term V, a significant difference in peak height between both cases can be seen after the first shock interaction. As already mentioned in the discussion of Fig. 6, this is caused by differences in initial flame thickness (see Fig. 8) and heat release τ_{h}, leading to a considerably increased density gradient for $\phi = 1$. Since the thickness of the lean flame is massively reduced after each shock interaction and the flame surface area is increased due to the formation of fresh gas funnels and other turbulent structures, the peak in baroclinic torque is massively increased at the re-shock, even surpassing the stoichiometric flame. The flame thickness decrease, is caused by the compression of the flame by the shock and the increased pressure level after passing of the shock wave. The flame thickness, which initially is about 8 times higher in the lean flame, is reduced by about 50% after interacting with the shock and re-shock (later interactions have a negligible effect on the flame thickness).

4.2 Fractal Analysis

A common approach for reaction rate closure in RANS and LES, is to model the sub-grid scale wrinkling factor $\Xi = \overline{|\nabla c|}/|\nabla \bar{c}|$ (overbar indicates RANS averaging or LES filtering) as a power-law function, giving the expression (Fureby, 2005, Knikker et al., 2004):

$$\Xi = (\eta_o/\eta_i)^{D_f-2} \tag{13}$$

The outer and inner cut-off scales η_o and η_i are taken as the LES filter width Δ and a quantity that corresponds to the smallest occurring flame structure (Gülder, 1995), respectively. The fractal dimension D_f of the premixed flame can be calculated from the present DNS data by explicit filtering (Chakraborty and Klein, 2008). With the generalized flame surface density (FSD) $\Sigma_{gen} = \overline{|\nabla c|}$ defined by Boger et al. (1998) and using Eq. (13) the following expression for Σ_{gen} is obtained (Gouldin et al., 1989):

$$\Sigma_{gen} = |\nabla \bar{c}|(\Delta/\eta_i)^{D_f-2} \tag{14}$$

Following the method described in detail by Chakraborty and Klein (2008) and taking the volume average of Eq. (14), results in

$$\log(\langle\Sigma_{gen}\rangle/\langle|\nabla \bar{c}|\rangle) = (D_f-2)\log(\Delta) - (D_f-2)\log(\eta_i)\ . \tag{15}$$

Equation (15) can be interpreted as a straight line equation with a slope of (D_f-2). Figure 9a shows a double logarithmic plot of $\langle\Sigma_{gen}\rangle/\langle|\nabla \bar{c}|\rangle$ over the normalized filter size Δ for the stoichiometric case at $t \times S_{L,st}/\delta_{th,st} = 1$. When the filter width is smaller than the stoichiometric flame thickness $\delta_{th,st}$ (see sec. 3), the variation of $\log(\langle\Sigma_{gen}\rangle/\langle|\nabla \bar{c}|\rangle)$ becomes increasingly non-linear. For $\Delta \gg \delta_{th,st}$ the linear behaviour expected from Eq. (15) becomes apparent and the fractal dimension D_f can be calculated from the slope of a line fit. By repeating this procedure for successive timesteps and for all cases, the evolution of D_f over time, as shown in Fig. 9b, can be determined. Since the definition of D_f is tied to the FSD or flame surface area A_f (see Eq. (9)), it is consistent that D_f evolves similarly to A_f as shown in Fig. 6a. Initially the shock will flatten the initially disturbed (see Fig. 4) flame surface, reducing the fractal dimension to $D_f \approx 2$, or $\Xi \approx 1$. The fractal dimension then steeply increases to about 2.92 for $\phi = 1$ and 2.78 for $\phi = 0.5$. After the re-shock D_f increases further for the lean case and reaches larger values than the stoichiometric mixture, with a maximum of ≈ 2.96 (≈ 2.89 for stoichiometric). Towards the end of the simulation the fractal dimension values settle at 2.38 ($\phi = 1$) and 2.67 ($\phi = 0.5$). For a passive interface in turbulence Kerstein (1988) predicts a fractal dimension of $7/3$, while the maximum D_f for a premixed flame is expected to be $8/3$ (Hawkes et al., 2012). Values of $D_f > 8/3$ are a strong indicator for additional wrinkling caused by the RMI and possibly thermo-diffusive instabilities for Le < 1.

5 Summary and Outlook

DNS of premixed lean and stoichiometric H2/Air flames interacting with a $M_s = 1.5$ shock-wave are performed. Two cases are investigated that involve a lean and a stoichiometric H2/Air mixture with an equivalence ratio of $\phi = 0.5$ and $\phi = 1$. Spatial discretization and shock capturing is achieved by implementing the WENO-5 scheme. The scheme successfully avoids numerical oscillations around discontinuities, while resolving the shock with about 2-3 grid points.

During a simulation there are three significant occurrences of shock-flame interaction:

- interaction of the shock-wave with the initially perturbed flame surface
- re-shock due to the reflection of the shock wave at the back wall
- interaction with partially reflected shock (flame surface $\leftrightarrow$ wall)

The individual terms of the enstrophy transport equation are investigated, where it is found that the baroclinic torque, which is responsible for the RMI, dominates the other terms most of the time. It is

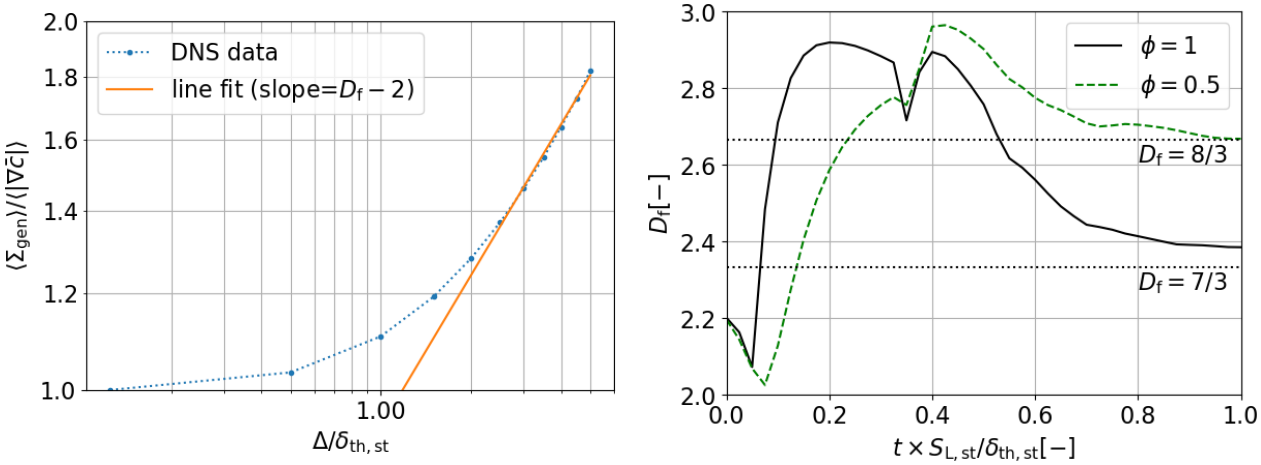

(a) Volume averaged wrinkling factor.

(b) Fractal dimension.

***Fig. 9**: Left: Double logarithmic plot of volume averaged wrinkling factor over normalized filter size, for $\phi = 1$ and $t \times S_{L,st}/\delta_{th,st} = 1$. Right: Fractal dimension for lean and stoichiometric gas mixture over time.*

found that the vortex stretching and diffusion term surpass the baroclinic term after the re-shock. This effect is visible in the lean case and to a lesser extent in the stoichiometric case as the vortex stretching and diffusion terms are generally much smaller there. The baroclinic torque shows high peaks after each shock-flame interaction. The peak heights are heavily influenced by the flame thickness, which differs between both cases and in time due to flame compression and an increased pressure level caused by the shock wave. After the first shock-flame interaction, the peak height of the stoichiometric case is about ten times higher than for the lean case, due to the previously mentioned differences in flame thickness and also heat release ratio, leading to an increased density gradient across the flame. After the re-shock the baroclinic torque production of the lean case increases significantly as the difference in flame thickness is reduced and more flame surface area is available.

The effects of the baroclinic torque production and flame wrinkling also become apparent when investigating the temporal development of the flame surface area A_f and the turbulent mixing width δ_m. A strong increase in A_f and δ_m is observed on each shock interaction, with a maximum possible increase of about 400% for the investigated cases. Due to funnel-closure and smoothing effects of the stoichiometric case, the end values of A_f differ by about 30% between both cases. Finally the fractal behavior of the flame surface is investigated in the context of power-law based modeling of the wrinkling factor. For the stoichiometric and lean case a maximum fractal dimension of about 2.92 to 2.96 is determined (reached at different times), before settling at 2.38 respective 2.67.

For the lean case (Le = 0.5) the Lewis number is significantly smaller than unity, therefore the flame is more susceptible to thermo-diffusive instabilities in addition to the RMI. A next step would be to investigate the effect of isolated changes in the Lewis number to separate the influence on flame wrinkling of the thermo-diffusive instabilities and RMI. Furthermore the investigations on the enstrophy transport equation and fractal behavior can be used in the work towards a sub-grid model of the RMI flame wrinkling.

Acknowledgements

The presented work is funded by the German Federal Ministry of Economic Affairs and Energy (BMWi) on the basis of a decision by the German Bundestag (project no. 1501574) which is gratefully acknowledged.

References

Bechtold, J. K., Matalon, M. (2001). *The Dependence of the Markstein Length on Stoichiometry*. Combustion and Flame, 127(1-2):1906–1913.

Boger, M., Veynante, D., Boughanem, H., Trouvé, A. (1998). *Direct Numerical Simulation Analysis of Flame Surface Density Concept for Large Eddy Simulation of Turbulent Premixed Combustion*. Symposium (International) on Combustion, 27(1):917–925.

Breitung, W., Chan, C., Dorofeev, S., Eder, A., Gelfand, B., Heitsch, M., Klein, R., Malliakos, A., Shepherd, J., Studer, E., Thibault, P. (2000). *Flame Acceleration and Deflagration-to-Detonation Transition in Nuclear Safety*. NEA/CSNI/R(2000)7.

Chakraborty, N., Klein, M. (2008). *A Priori Direct Numerical Simulation Assessment of Algebraic Flame Surface Density Models for Turbulent Premixed Flames in the Context of Large Eddy Simulation*. Physics of Fluids, 20(8):085108.

Ciccarelli, G., Dorofeev, S. (2008). *Flame acceleration and Transition to Detonation in Ducts*. Progress in Energy and Combustion Science, 34(4):499–550.

Ciccarelli, G., Johansen, C. T., Parravani, M. (2010). *The Role of Shock–Flame Interactions on Flame Acceleration in an Obstacle Laden Channel*. Combustion and Flame, 157(11):2125–2136.

Dorofeev, S. B. (2011). *Flame Acceleration and Explosion Safety Applications*. Proceedings of the Combustion Institute, 33(2):2161–2175.

Fureby, C. (2005). *A Fractal Flame-Wrinkling Large Eddy Simulation Model for Premixed Turbulent Combustion*. Proceedings of the Combustion Institute, 30(1):593–601.

Goodwin, D. G., Speth, R. L., Moffat, H. K., Weber, B. W. (2018). *Cantera: An object-oriented software toolkit for chemical kinetics, thermodynamics, and transport processes*. `https://www.cantera.org`. Version 2.4.0.

Gouldin, F., Bray, K., Chen, J.-Y. (1989). *Chemical Closure Model for Fractal Flamelets*. Combustion and Flame, 77(3-4):241–259.

Gülder, O. (1995). *Inner Cutoff Scale of Flame Surface Wrinkling in Turbulent Premixed Flames*. Combustion and Flame, 103(1-2):107–114.

Hasslberger, J. (2017). *Numerical Simulation of Deflagration-to-Detonation Transition on Industry Scale*. Ph.D. thesis, Technical University Munich.

Hawkes, E. R., Chatakonda, O., Kolla, H., Kerstein, A. R., Chen, J. H. (2012). *A Petascale Direct Numerical Simulation Study of the Modelling of Flame Wrinkling for Large-Eddy Simulations in Intense Turbulence*. Combustion and Flame, 159(8):2690–2703.

Jenkins, K. W., Cant, R. S. (1999). *Direct Numerical Simulation of Turbulent Flame Kernels*. In Knight, D., Sakell, L., editors, *Recent Advances in DNS and LES*, pages 191–202. Springer Netherlands, Dordrecht.

Jiang, G.-S., Shu, C.-W. (1996). *Efficient Implementation of Weighted ENO Schemes*. Journal of Computational Physics, 126(1):202–228.

Kerstein, A. R. (1988). *Fractal Dimension of Turbulent Premixed Flames*. Combustion Science and Technology, 60(4-6):441–445.

Klein, M., Herbert, A., Kosaka, H., Böhm, B., Dreizler, A., Chakraborty, N., Papapostolou, V., Im, H. G., Hasslberger, J. (2020). *Evaluation of Flame Area Based on Detailed Chemistry DNS of Premixed Turbulent Hydrogen-Air Flames in Different Regimes of Combustion*. Flow, Turbulence and Combustion, 104(2-3):403–419.

Knikker, R., Veynante, D., Meneveau, C. (2004). *A Dynamic Flame Surface Density Model for Large Eddy Simulation of Turbulent Premixed Combustion*. Physics of Fluids, 16(11):L91–L94.

Lindl, J. (1995). *Development of the Indirect-Drive Approach to Inertial Confinement Fusion and the Target Physics Basis for Ignition and Gain*. Physics of Plasmas, 2(11):3933–4024.

Meshkov, E. E. (1972). *Instability of the Interface of Two Gases Accelerated by a Shock Wave*. Fluid Dynamics, 4(5):101–104.

Poinsot, T., Veynante, D. (2005). *Theoretical and Numerical Combustion*. Prog. Energy Combust. Sci., 28.

Rayleigh (1882). *Investigation of the Character of the Equilibrium of an Incompressible Heavy Fluid of Variable Density*. Proceedings of the London Mathematical Society, s1-14(1):170–177.

Remington, B. A., Drake, R. P., Takabe, H., Arnett, D. (2000). *A review of Astrophysics Experiments on Intense Lasers*. Physics of Plasmas, 7(5):1641–1652.

Richtmyer, R. D. (1960). *Taylor Instability in Shock Acceleration of Compressible Fluids*. Communications on Pure and Applied Mathematics, 13(2):297–319.

Shu, C.-W. (1998). *Essentially Non-Oscillatory and Weighted Essentially Non-Oscillatory Schemes for Hyperbolic Conservation Laws*. In *Advanced Numerical Approximation of Nonlinear Hyperbolic Equations*, pages 325–432. Springer.

Taylor, G. (1950). *The Instability of Liquid Surfaces when Accelerated in a Direction Perpendicular to their Planes. I.* Proceedings of the Royal Society of London. Series A. Mathematical and Physical Sciences, 201(1065):192–196.

Tritschler, V. K., Hickel, S., Hu, X. Y., Adams, N. A. (2013). *On the Kolmogorov Inertial Subrange Developing from Richtmyer-Meshkov Instability*. Physics of Fluids, 25(7):071701.

Tritschler, V. K., Olson, B. J., Lele, S. K., Hickel, S., Hu, X. Y., Adams, N. A. (2014). *On the Richtmyer–Meshkov Instability Evolving from a Deterministic Multimode Planar Interface*. Journal of Fluid Mechanics, 755:429–462.

Wray, A. A. (1990). *Minimal Storage Time Advancement Schemes for Spectral Methods*. NASA Ames Research Center, California, Report No. MS, 202.